

Effect of Jahn-Teller distortion on magnetic ordering in Dy(Fe,Mn)O₃ perovskitesF.-K. Chiang,^{1,2,3} M.-W. Chu,^{1,*} F. C. Chou,^{1,4} H. T. Jeng,⁵ H. S. Sheu,⁴ F. R. Chen,³ and C. H. Chen^{1,5}¹Center for Condensed Matter Sciences, National Taiwan University, Taipei 106, Taiwan²Taiwan International Graduate Program, Academia Sinica, Taipei 115, Taiwan³Department of Engineering and System Science, National Tsing Hua University, Hsinchu 300, Taiwan⁴National Synchrotron Radiation Research Center, Hsinchu 300, Taiwan⁵Institute of Physics, Academia Sinica, Taipei 115, Taiwan

(Received 28 January 2011; revised manuscript received 8 April 2011; published 6 June 2011)

The structural, magnetic properties of the rare-earth perovskites, DyFe_{1-x}Mn_xO₃ (space group, orthorhombic *Pbnm*), were studied, and the magnetic phase diagram of the solid solution was investigated, which unveiled an unexplored hidden field-induced weak ferromagnetism in the material system with $x = 0.5-0.9$ (antiferromagnetically ordered along the *b* axis and canted along the *c* axis). In the solid solution, the Jahn-Teller distortion contributed by Mn³⁺ gives rise to the predominance of the *bc* plane sublattice with increasing Mn and also the *effective onset of orbital ordering in the ab plane* for $x = 0.5$ and above. These distinct features in the respective lattice and orbital degrees of freedom induce the Dy-(Fe,Mn) electronic interaction anisotropy primarily in the *bc* plane and the growing in-(*ab*)plane electronic anisotropy, effectively competing with each other above $x = 0.5$. The close entanglement of these anisotropies introduced by the various lattice, orbital, and correlated electronic characters results in the favoring of the Dzyaloshinskii-Moriya interaction dictating along the *a* axis, in contrast to the conventionally observed *b* axis and accounting for the hidden field-induced canted magnetic ordering in the *bc* plane. The complex interplays of these multiple factors are discussed in this work and satisfactorily explain the rich magnetic phase diagram of the solid solution.

DOI: [10.1103/PhysRevB.83.245105](https://doi.org/10.1103/PhysRevB.83.245105)

PACS number(s): 71.27.+a, 75.47.Lx, 75.25.Dk, 61.50.Ks

I. INTRODUCTION

The structure of rare-earth perovskite oxides, RMO₃ (*R*, rare earth; *M*, transition metal; space group, orthorhombic *Pbnm*), is primitively described by the GdFeO₃-type distortion, which determines the tilting of corner-shared MO₆ octahedra from the *ab* plane and the rotation of those around *c* axis ($c \sim \sqrt{2}a, b$) as a result of the relatively smaller ionic size of *R* at the crystallographic site.^{1,2}

In RMnO₃ perovskite manganites, the crystal-field characteristic to the octahedral symmetry splits the electronic configuration of Mn³⁺ ($3d^4$) to $t_{2g}^3 e_g^1$ and the Hund's-rule coupling dictates a ferromagnetic (FM) coupling for the t_{2g}^3 and e_g^1 electrons (thus $S = 2$ and $Mn^{3+} = 4\mu_B$, where μ_B is the Bohr magneton).¹⁻⁴ The double degeneracy of the e_g orbitals is lifted by the singly occupied e_g^1 through Jahn-Teller (JT) distortion.¹⁻³ The JT distortion manifests the displacements of coordinated oxygen ions away from Mn³⁺, resulting in a low-energy e_g level that accordingly removes the orbital degeneracy.¹⁻³ The thus-induced elongated Mn-O bonds would tend to align with the occupied e_g^1 orbitals due to the electron-phonon coupling essence of the JT distortion.^{2,3} Indeed, the staggered e_g^1 -orbital ordering in the *ab* plane in RMnO₃ (*R* = La-Lu) perovskites is considerably attributed to the JT distortion,³⁻⁵ establishing the entanglement of the JT distortion and orbital degree of freedom in manganites.¹⁻⁵ Moreover, this entanglement coupled with the primitive GdFeO₃-type distortion of the lattice gives rise to an increased structural distortion, which mediates a narrowing of the e_g bands and an increase in e_g^1 electron localizations that favor antiferromagnetic (AFM) superexchange interactions, altogether impacting on the magnetic and transport properties of manganites.¹⁻³ The rich magnetic phase diagram of RMnO₃

(*R* = La-Lu) perovskites with insulating, orbital-ordered characteristics represents a classical example, which requires further elucidations.^{4,5}

In LaMnO₃ (featuring the largest R^{3+} size in the RMnO₃ family),^{4,5} the staggered orbital ordering in the *ab* plane induces an in-(*ab*)plane anisotropy and a two-dimensional-like electronic character, contributing to the in-plane FM interaction and the interplane AFM coupling of the material, i.e., the *A*-type AFM ground state.^{1,3-5} With the continuous decrease in R^{3+} sizes from La to Lu in the family, the GdFeO₃-type distortion is readily enhanced and grown into the predominant factor in the lattice degree of freedom compared to the JT distortion.^{4,5} This structural feature affects the delicate exchange interactions and is correlated with the onset of otherwise *E*-type AFM ordering (up-up-down-down spin coupling along the [110] axis in the *ab* plane) in the small R^{3+} regime of HoMnO₃ to LuMnO₃.^{4,5} In the relatively large R^{3+} regime of RMnO₃ (*R* = Pr-Gd), the *A*-type AFM ordering persists.^{4,5} A narrow window with a distinct incommensurate spiral magnetic ordering in the *bc* plane, however, opens for TbMnO₃ and DyMnO₃ with a relatively medium R^{3+} size.⁶⁻⁸ In TbMnO₃ and DyMnO₃, the associated compromised GdFeO₃-type distortion, the JT distortion, and the orbital ordering cooperatively result in the frustrated superexchange interactions in the *ab* plane to facilitate the spiral ordering.^{4,9} This spiral ordering breaks the spatial reversal symmetry and leads to the onset of ferroelectricity in both materials with the assist of the Dzyaloshinskii-Moriya (DM) interaction (later in Sec. III B) or the spin current mechanism.^{8,10-13} Materials showing such an intimate coupling between the ferroelectricity and the ordered magnetic ground state are nowadays known as multiferroics.^{8,10-13}

The complex interplays of charge, orbital, lattice, and spin degrees of freedom above are unambiguously central

to the physics of manganites and these multiple degrees of freedom are all correlated with the electronic characteristics of Mn^{3+} .¹⁻⁵ A systematic exploration for the frontiers of rare-earth manganites thus does not expect a direct alloying for Mn,¹ rather through solid solutions on *R*, such as the discovery of colossal magnetoresistance in $(\text{La}^{3+}, \text{Sr}^{2+})\text{MnO}_3$ and $(\text{Nd}^{3+}, \text{Sr}^{2+})\text{MnO}_3$.^{1,3} Nevertheless, it is not excluded that solid solutions on the Mn site may lead to unexpected dimensions in physics of the materials, though indeed much less discussed before.^{1,14,15}

Here, we report a thorough magnetic phase diagram study of $\text{Dy}(\text{Fe}, \text{Mn})\text{O}_3$ through elaborate structural and magnetic characterizations of the materials, unveiling a hidden field-induced canted AFM ordering (weak ferromagnetism, WFM) in the *bc* plane and the essential role played by the JT distortion in this magnetic ground state. For Fe^{3+} , the high-spin electronic configuration of $t_{2g}^3 e_g^2$ ($S = 5/2$; $\text{Fe}^{3+} = 5\mu_B$) determines a practically doubly degenerate state for the half-occupied e_g orbitals.^{14,16,17} The orbital degree of freedom and JT distortion characteristic to Mn^{3+} are thus quenched in Fe^{3+} ,^{16,17} giving rise to a simpler description of the solid solution when starting from the parent-phase side of DyFeO_3 . Hereinafter, we denote the solid solution as $\text{DyFe}_{1-x}\text{Mn}_x\text{O}_3$ ($x = 0, 0.1, 0.2-1.0$) and discuss the structural, magnetic properties accordingly within the context of the essential physics above, interplay of the multiple degrees of freedom in the materials. It is worth mentioning that DyFeO_3 was recently reported as a multiferroic material with an alternative origin of the magnetostriction between Dy^{3+} and Fe^{3+} ,^{16,17} although multiferroics is rather beyond the scope of this work.

II. EXPERIMENTAL

The powder samples of the solid solution, $\text{DyFe}_{1-x}\text{Mn}_x\text{O}_3$ ($x = 0, 0.1, 0.2-1$), were synthesized using the reported sol-gel method¹⁸ with Dy acetylacetonate hydrate, Mn acetylacetonate, and Fe acetylacetonate as the starting chemicals and finally annealed at 1400 °C for 4 h in air. The sol-gel synthesis is well known for its facile control over stoichiometry and homogeneity compared to the conventional solid-state reaction.^{18,19} The stoichiometry and homogeneity of each material in the solid solution were confirmed by quantitative energy-dispersive x-ray spectroscopy in a transmission electron microscope (TEM; FEI Tecnai F20, 200 kV) for 30 individual crystals of each material and by inductively coupled plasma (ICP) analyses. The phase purity and the structural characteristic of each material were investigated by Rietveld refinements of powder x-ray diffraction (XRD) patterns, acquired at room temperature with a synchrotron radiation source (wavelength, 0.62 Å) at National Synchrotron Radiation Research Center in Taiwan. The Rietveld analyses were performed using the General Structure Analysis System (GSAS) program. The magnetic characterizations of the *powders* were conducted on a superconducting quantum interference device magnetometer (SQUID, Quantum Design). For also tackling the electronic hybridizations of the materials, studies of the density of states (DOS) of the oxygen K edge above Fermi level using core-level electronic excitations represent a classical approach.²⁰⁻²² The core-level spectroscopy was performed

by electron energy-loss spectroscopy (EELS) installed in the TEM also equipped with an electron monochromator, achieving an energy resolution of ~ 0.2 eV.

III. RESULTS AND DISCUSSION

A. Structural characterizations

The careful Rietveld analyses of the XRD powder patterns of the solid solution indicate that all synthesized materials crystallize in the perovskite phase with a space group of *Pbnm*, primitive to rare-earth perovskites,^{1,2} with superb phase purity and crystallinity as revealed in the representative Rietveld plot of $\text{DyFe}_{0.5}\text{Mn}_{0.5}\text{O}_3$ [Fig. 1(a)]. The refinement results are also given in Table I. Figure 1(b) shows the evolution of the cell parameters (*a*, *b*, and, $c\sqrt{2}$) and volume (*V*) as a function of compositions in $\text{DyFe}_{1-x}\text{Mn}_x\text{O}_3$. The increase (decrease) in the *b* axis (*c* axis) toward DyMnO_3 , $x = 1$, is remarkable, accompanied with a sizable increase in the cell volume, while the *a* axis is only gently reduced. Such a cell-parameter tendency indicates that the lattice degree of freedom in the solid solution should be predominated by the *bc* plane upon approaching DyMnO_3 ($x = 1$). The increase in the cell volume further reveals that the *c*-axis reduction is largely overwhelmed by the *b*-axis elongation. It should be noted that these structural

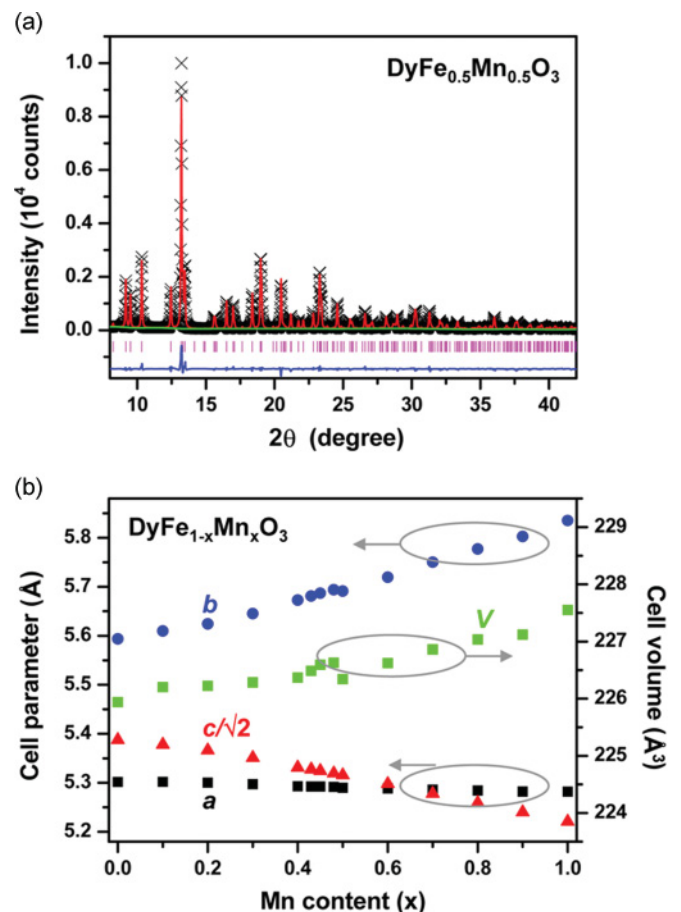


FIG. 1. (Color online) (a) The Rietveld-refinement plot of $\text{DyFe}_{0.5}\text{Mn}_{0.5}\text{O}_3$ in the space group of *Pbnm*. (b) The evolutions of the cell parameters (*a*, *b*, and, $c\sqrt{2}$) and cell volume (*V*) as a function of compositions in the $\text{DyFe}_{1-x}\text{Mn}_x\text{O}_3$ solid solution.

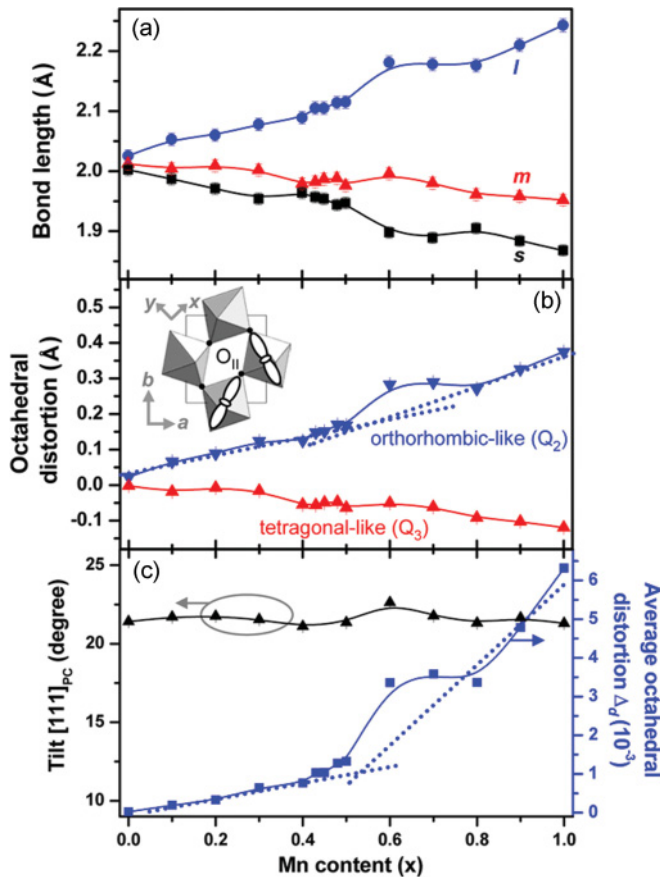


FIG. 2. (Color online) (a) The composition-dependent variations of the M-O bonds in the MO_6 octahedra with l , s , and m denoting the long, short M-O_{II} bonds and the middle-length M-O_I bonds, respectively. O_I (O_{II}) represents the apical (equatorial) oxygen along the c axis [in the ab plane, inset of (b)]. (b) The in- (ab) plane orthorhombic- and out-of-plane tetragonal-like distortions of the octahedra characterized by Q_2 and Q_3 , respectively. Dotted lines guiding Q_2 point to the slope crossover as a result of the effective onset of orbital ordering at $x \sim 0.5$ (see text). Inset, the projected room-temperature crystal structure of DyMnO_3 along the c axis with the corresponding staggered orbital ordering in the ab plane schematized in only two of the octahedra at the right-bottom side for simplicity. Dy in the structure is also ignored for simplicity. (c) The average tilt angle of the octahedra around the pseudocubic (PC) [111] direction estimating the GdFeO_3 -type distortion, and the average octahedral distortion evaluated by Δ_d . Dotted lines guiding Δ_d direct to the effective onset of orbital ordering around the slope changeover at $x \sim 0.5$ (see text). Error bars in (a)–(c), estimated standard deviations (0.5% of the corresponding data) derived from the respective Rietveld refinements. The error bars for Δ_d , though shown, are invisible in the scale of the figure.

characteristics cannot be explained within the context of the classical ionic-size consideration, since the high-spin Fe^{3+} and Mn^{3+} are both ~ 0.645 Å in ionic radius.²³ To capture the underlying origins for these derived features, a detailed structural examination was performed below.

Figure 2 was derived from the Rietveld refinement results. Figure 2(a) exhibits the composition-dependent variations of the M-O bonds ($\text{M} = \text{Fe}, \text{Mn}$) in the MO_6 octahedra

with l , s , and m denoting the long and short M-O_{II} bonds predominantly in the ab plane, and the middle-length M-O_I bonds predominantly along the c axis, respectively. O_I (O_{II}) stands for the apical (equatorial) oxygen coordinating the octahedra along the c axis [in the ab plane; inset, Fig. 2(b)], also elucidated in Table I. In DyFeO_3 [$x = 0$, Fig. 2(a)], the similar lengths of the l , s , and m bonds are correlated with the quenched orbital degree of freedom and JT distortion for Fe^{3+} and are characteristic to the material.^{16,17,24} By contrast, DyMnO_3 ($x = 1$) exhibits a much more distorted structure with a large difference among l , s , and m [Fig. 2(a)]. In DyMnO_3 [projected structure along the c axis, inset in Fig. 2(b)], the $d_{3x^2-r^2}/d_{3y^2-r^2}$ -staggered orbital ordering in the ab plane (inset, denoted in only two of the four octahedra at the right-bottom side for simplicity) is well known to superimpose with the alternating ordering pattern of the JT-induced elongated l bonds (inset, see the top-left two octahedra without the orbital denotation for clarity).^{4,5,25} It has been established that orbital ordering can be structurally revealed when coupled to the lattice degree of freedom by the JT distortion and inducing long M-O bonds,^{3,4} i.e., the present case of DyMnO_3 [inset, Fig. 2(b)].^{4,5} In the solid solution [Fig. 2(a)], the increase in l towards DyMnO_3 is then clearly attributed to the JT distortion pristine to Mn^{3+} ,¹⁻⁵ and could also be regarded as a ready buildup of the orbital ordering, which will be discussed further in Fig. 2(c). The drastic decrease in s accompanied with the increasing l [Fig. 2(a)] is also characteristic to the JT distortion in manganites.^{5,21,26,27} The corresponding reduction of the m length [Fig. 2(a)] indicates an otherwise increasing distortion along the c axis upon the JT distortion.

Figure 2(b) shows the in- (ab) plane orthorhombic- and out-of-plane tetragonal-like distortions of the octahedra typically characterized by Q_2 [$= (l - s)$] and Q_3 [$= (2m - l - s)/\sqrt{3}$] vibration phonon modes, respectively.^{5,28,29} In DyFeO_3 [$x = 0$, Fig. 2(b)], both Q_2 and Q_3 are nearly zero as expected from the analogous l , s , and m in Fig. 2(a).²⁴ Toward DyMnO_3 [$x = 1$, Fig. 2(b)], the increase in Q_2 is associated with the effect of the JT distortion [Fig. 2(a)] and the decrease in Q_3 indeed reveals the onset of an out-of-plane distortion (along the c axis) along with the JT distortion. Upon approaching DyMnO_3 , the positive sign of Q_2 and the primarily b -oriented l bonds [Fig. 2(b) and inset] indicate that the predominant lattice degree of freedom associated with the JT distortion is along the b axis. For Q_3 [Fig. 2(b)], the negative sign and slope indicate that the distortion along the c axis is competing with that of the JT distortion primarily along the b axis. It is thus unambiguous that the lattice degree of freedom in the solid solution is most prominently determined by the bc -plane sublattice. In addition, the overall larger magnitude of Q_2 over Q_3 [Fig. 2(b)] provides a direct understanding for the decrease in the c axis visibly overwhelmed by the increase in the b axis, derived earlier from the macroscopic cell-volume increase in Fig. 1(b).

In the solid solution, the GdFeO_3 -type distortion, featuring the primitive lattice degree of freedom in rare-earth perovskites,^{1,2} can be estimated by the average tilt angle of the octahedra around the pseudocubic [111] direction [Fig. 2(c)] taking into account both the in-plane, $\text{M-O}_{\text{II}}\text{-M}$, and out-of-plane, $\text{M-O}_I\text{-M}$, bond angles.^{30,31} In Fig. 2(c), the change in the average tilt angle, i.e., the GdFeO_3 -type distortion in

TABLE I. The representative Rietveld refinement results of $\text{DyFe}_{1-x}\text{Mn}_x\text{O}_3$ (space group, $Pbnm$). Crystallographic sites: Dy, $4c$ ($x,y,1/4$), site symmetry m ; M (Fe,Mn), $4b$ ($1/2,0,0$), site symmetry $\bar{1}$; O_I , $4c$ ($x,y,1/4$), site symmetry m ; O_{II} , $8d$ (x,y,z), site symmetry 1 . O_I , the apical oxygen connecting the corner-shared octahedra along the c axis; O_{II} , the equatorial oxygen connecting the octahedra in the ab plane; and B_{iso} , the isotropic atomic displacement parameters.

$\text{DyFe}_{1-x}\text{Mn}_x\text{O}_3$	$x = 0.1$	$x = 0.3$	$x = 0.5$	$x = 0.7$	$x = 0.9$
a (Å)	5.3018(1)	5.2971(1)	5.2898(1)	5.2859(1)	5.2819(1)
b (Å)	5.6097(1)	5.6451(1)	5.6911(1)	5.7501(1)	5.8026(1)
c (Å)	7.6056(1)	7.5674(1)	7.5171(1)	7.4639(1)	7.4104(1)
V (Å ³)	226.20	226.28	226.30	226.86	227.12
x (Dy)	-0.0175(2)	-0.0178(2)	-0.0179(2)	-0.0184(2)	-0.0178(2)
y (Dy)	0.0672(3)	0.0700(1)	0.0733(3)	0.0711(1)	0.0806(1)
B_{iso} (Dy)	0.8(2)	1.3(2)	0.9(2)	1.4(2)	1.2(3)
B_{iso} (M)	1.0(2)	1.4(3)	1.0(2)	1.4(4)	1.3(2)
x (O_I)	0.111(2)	0.117(2)	0.109(2)	0.119(2)	0.114(2)
y (O_I)	0.459(2)	0.464(2)	0.465(2)	0.466(2)	0.467(2)
B_{iso} (O_I)	1.6(1)	1.8(2)	1.4(2)	1.7(2)	1.5(2)
x (O_{II})	0.697(2)	0.705(2)	0.700(2)	0.712(2)	0.711(2)
y (O_{II})	0.312(2)	0.306(2)	0.314(2)	0.318(2)	0.322(2)
z (O_{II})	0.059(1)	0.054(1)	0.053(1)	0.052(1)	0.052(1)
B_{iso} (O_{II})	1.6(2)	1.8(2)	1.4(2)	1.7(2)	1.5(2)
R_{wp} (%)	6.7	8.1	5.5	7.7	7.9
R_p (%)	4.8	6.4	3.6	6.0	6.2
χ^2	1.2	1.3	1.2	1.1	1.2

effect,^{30,31} is negligible throughout the solid solution. The above predominant lattice degree of freedom by the bc -plane sublattice then arises from a major contribution of the JT distortion.

The further examination of the average octahedral distortion Δ_d [$= (1/6) \sum_{n=1-6} [(d_n - \langle d \rangle) / \langle d \rangle]^2$, where d_n ($\langle d \rangle$) is the individual (average) M -O bond length] is shown in Fig. 2(c). Compared to Q_2 and Q_3 [Fig. 2(b)], this structural characteristic more statistically evaluates the JT distortion.^{5,29,30} Figure 2(c) indicates an intriguing slope changeover around $x \sim 0.5$ (guided by the dotted lines), also principally revealed in Q_2 [see also the dotted lines in Fig. 2(b)]. Considering the Δ_d -slope interpolation from $x \sim 1$ for the phases to the right of $\text{DyFe}_{0.5}\text{Mn}_{0.5}\text{O}_3$ [Fig. 2(c)] and the entanglement of the JT distortion and ab -plane staggered orbital ordering in DyMnO_3 ($x = 1$),^{4,5,25} this slope crossover can be understood as an effective onset of orbital ordering coupled to the sizable JT distortion for $x \geq 0.5$ [see the guiding dotted lines for Q_2 , Fig. 2(b)]. The above predominance of the bc -plane sublattice due to the JT distortion is accordingly conjugated with the effective orbital-ordered onset in the ab plane for phases with $x \geq 0.5$ and also most prominent in these high-Mn materials as indicated from the corresponding steep Δ_d slope in Fig. 2(c). As established below, these lattice and orbital characteristics closely affect the magnetic ordering in the solid solution.

B. Magnetic and EELS spectroscopic characterizations

Figure 3(a) shows the temperature (T)-dependent magnetization (M) curves of the solid solution and Fig. 3(b) exhibits the zero-field-cooled (blue) and field-cooled (red) M - T curves of the powder samples with $x = 0.4$ – 0.6 . Figure 3(c) depicts the isothermal field-dependent M characteristics of the powder samples with $x = 0.5$ and 0.6 . The derived magnetic

phase diagram from Fig. 3 is shown in Fig. 4(a) with the relevant magnetic orderings of DyFeO_3 and $\text{DyFe}_{0.5}\text{Mn}_{0.5}\text{O}_3$ schematized in Figs. 4(b) and 4(c), respectively.

In the M - T feature of DyFeO_3 [Fig. 3(a)], the broad maximum accompanied with a gradual, diffused downturn in front of the intense Dy^{3+} -paramagnetic (PM) tail raising at ~ 25 K results from the characteristic spin-reorientation transition of this material.^{16,32–34} As reported, the corresponding transition temperature (T_R) can be derived around the indicated valley (arrow), ~ 35 K, also in good agreement with the literature.^{14,16,32–34} In addition, DyFeO_3 is characterized by a PM-to-WFM transition at ~ 645 K (T_N), below which the Fe^{3+} magnetic sublattice (coincident with the crystallographic lattice) displays a G -type AFM ordering [both in- (ab) and interplane antiparallel spin couplings] along the a axis and slightly canted along the c axis, leading to the associated WFM [$G_x F_z$ in Bertaut's magnetic notation, Fig. 4(b)].^{32–34} Below T_R (~ 35 K), Fe^{3+} spins reorient from a - ($G_x F_z$) to the b axis in an otherwise collinear G -type AFM form (G_y in Bertaut's notation) due to the increasing magnetic anisotropy applied by Dy^{3+} on the Fe^{3+} magnetic sublattice at low temperatures.^{32–34} In effect, the WFM state in DyFeO_3 is a direct consequence of the DM interaction on the primitive G -type ordering along the a axis.^{32–34} The DM interaction represents the antisymmetric coupling component of the anisotropic AFM superexchange interactions in Fe^{3+} , formulated as $D \cdot (S_i \times S_j)$ with D denoting the DM vector and $S_{i,j}$ the spins on the nearest-neighbor (NN) transition-metal sites i and j .³⁵ Considering this DM formulation and taking into account the primitive AFM ordering along the a axis in DyFeO_3 , the DM vector (D) is then along the b axis and the antisymmetric electronic contributions to the anisotropic exchange interactions lie in the orthogonal plane,^{35,36} i.e., the ac plane, leading to the observed spin canting along the c axis [$G_x F_z$, Fig. 4(b)].^{32–34}

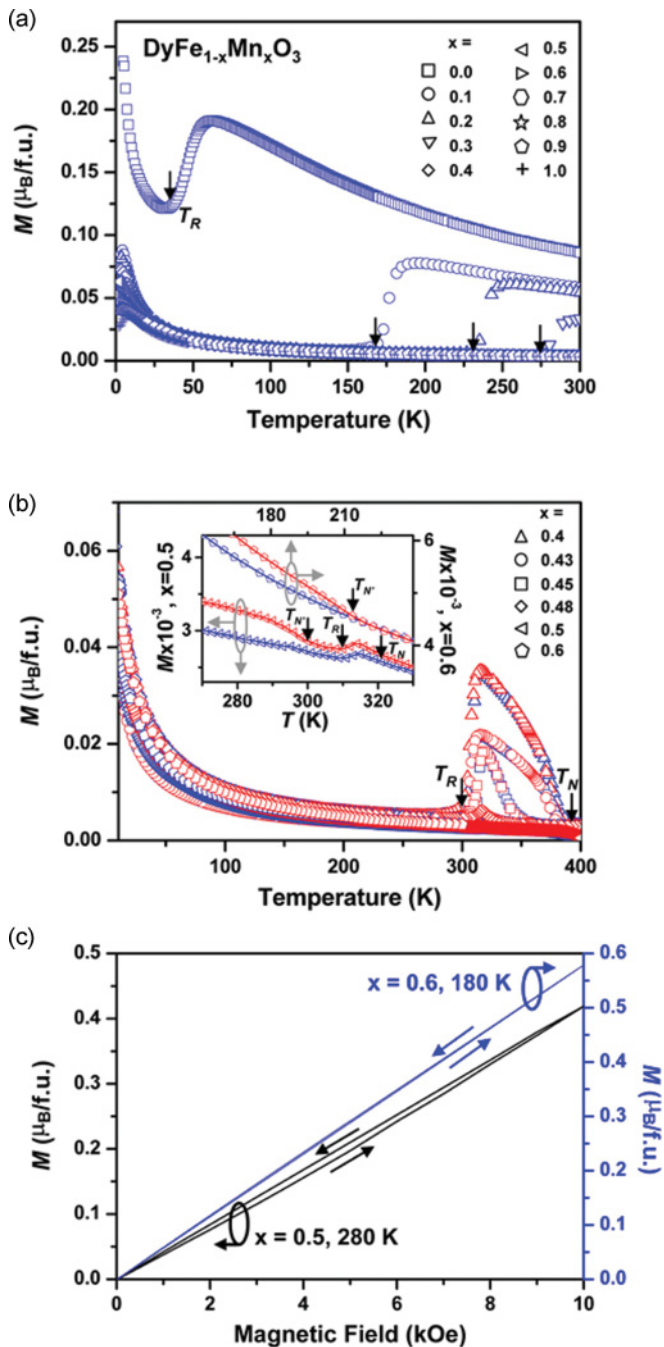


FIG. 3. (Color online) (a) The temperature (T)-dependent magnetization (M) curves of the solid solution at an applied field of 100 Oe. T_R (arrows): the spin-reorientation transition temperature. (b) The zero-field-cooled (blue) and field-cooled (red) M - T curves of the powder samples with $x = 0.4$ – 0.6 in the solid solution at an applied field of 100 Oe. Inset: the blowup for part of the M - T curves of $x = 0.5$ and 0.6 . T_N and $T_{N'}$: the transition temperatures for WFM ($G_x F_z$) ordering in the ac plane and FI-WFM state in the bc plane, respectively. (c) The isothermal field-dependent M curves of the powder samples with $x = 0.5$ and 0.6 acquired at 280 and 180 K (both below $T_{N'}$), respectively.

The essential ingredient to achieve the DM interaction is notably the lifting of an inversion symmetry interconnecting S_i and S_j through the off-center displacement of the coordinated

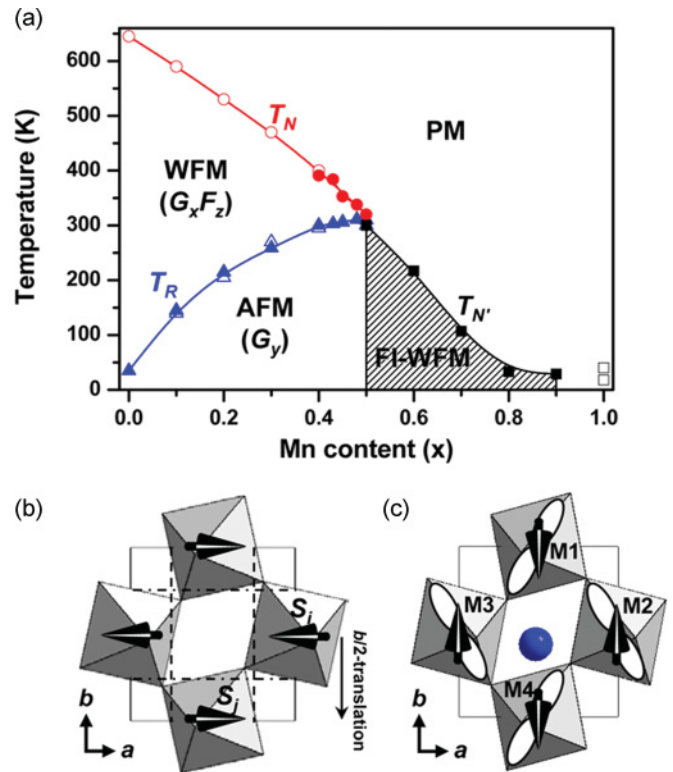


FIG. 4. (Color online) (a) The magnetic phase diagram of the $DyFe_{1-x}Mn_xO_3$ solid solution derived from Fig. 3 (closed symbols). Open symbols: reproduced from Ref. 14 (those of $DyMnO_3$ from Ref. 7). (b) The schematic WFM ($G_x F_z$) ordering in $DyFeO_3$ superimposed with the c -projected room-temperature crystal structure.²⁴ Dy in the structure is ignored for simplicity and the arrows with a white-shadowed head signify the canted spins out of the paper plane, corresponding to $G_x F_z$.³⁶ Dashed lines: the b -glide planes specific to $Pbnm$. The corresponding $b/2$ -translation operation is also shown. Dotted-dashed lines: the n -glide planes specific to the space group. (c) The schematic FI-WFM ordering in the bc plane of $DyFe_{0.5}Mn_{0.5}O_3$ ($x = 0.5$) superimposed with the c -projected room-temperature crystal structure (Table I). The effective onset of orbital ordering in the ab plane at $x \sim 0.5$ is also schematized and the arrows with a white-shadowed head signify the canted spins out of the paper plane. Blue atom: Dy. M1–M4: see the inset of Fig. 5(a).

atom in the middle (i.e., oxygen in $DyFe_{1-x}Mn_xO_3$), and D is always perpendicular to $S_{i,j}$ ($D \perp S_{i,j}$).^{10,16,35} In $DyFeO_3$, this essential inversion-symmetry breakdown is natively facilitated by O_{II} due to its crystallographically allowed off-center displacements along the a , b , and c axes [null site symmetry, (x,y,z) ;³⁷ also Table I]. Indeed, such off-center displacements of O_{II} result in the deviation from an otherwise $M-O_{II}-M$ angle of 180° in the ab plane of $DyFeO_3$ [see the c -projected room-temperature structure,²⁴ Fig. 4(b)]. While an off-center displacement is also allowed for O_I in the ab plane [mirror (m) site symmetry, $(x,y,1/4)$;³⁷ also Table I], the inversion symmetry $\bar{1}$ bound to the transition-metal chains along the c axis (Ref. 37; also Table I) appears to counterbalance with this off-center tendency of O_I . From these crystallographic points of view for $Pbnm$, O_{II} connecting the octahedra in the ab plane should be the most important factor for the DM interaction. The associated O_{II} displacements are correlated

with the inversion-symmetry breakdowns along the a and b axes, crystallographically described by the respective b and n glides.^{36,37} The b -glide plane [dashed lines, Fig. 4(b)] practically bisects two NN octahedra in the ab plane and is perpendicular to the a axis.³⁷ The operation of this symmetry element is further described, for example, by mirroring S_i to the NN S_j along the a axis after the indicated $b/2$ translation of the S_i -specific octahedron in Fig. 4(b).^{36,37} This mirrorlike operation forbids inversion symmetry along the a axis and accordingly, favors the relation of $D \parallel b$ axis for $S_{i,j}$ along the a axis as observed in WFM of DyFeO₃ [$G_x F_z$, Fig. 4(b)].³⁶ Moreover, the n -glide plane [dotted-dashed lines, Fig. 4(b)] is orthogonal to the b axis and shares a similar mirrorlike operation essence to the NN $S_{i,j}$ sites,^{36,37} thus implying a relation of $D \parallel a$ axis. Nevertheless, it is not possible to resolve this relation of $D \parallel a$ axis in the WFM state of DyFeO₃ ($G_x F_z$) considering that D is otherwise parallel to the G_x -ordered Fe³⁺ spins along the a axis, at odds with the DM criterion of $D \perp S_{i,j}$.³²⁻³⁵

Now, we turn to the magnetic transitions in the full solid solution. In the solid solution, T_R [arrows, Fig. 3(a)] indicating the spin-reorientation transition to G_y type increases from ~ 35 K in DyFeO₃ ($x = 0$) to ~ 300 K in the phase with $x = 0.4$ [T_R , Fig. 3(b)].¹⁴ By contrast, T_N underlining the WFM ($G_x F_z$) transition decreases from ~ 645 K in DyFeO₃ [Fig. 4(a)] to ~ 390 K in $x = 0.4$ [T_N , Fig. 3(b)], altogether showing a merging tendency for T_N and T_R in the phase diagram [Fig. 4(a)].¹⁴ With slightly higher Mn concentrations [$x = 0.43, 0.45, 0.48, \text{ and } 0.5$; Fig. 3(b)], T_N and T_R , however, do not coincide with each other [see Fig. 4(a) and more clearly the inset of Fig. 3(b) for $x = 0.5$]. Instead, a hysteresis feature reflecting a FM-like character¹⁵ appears in $x = 0.5$ below ~ 300 K [inset, Fig. 3(b)]. In $x = 0.6-0.9$, T_N and T_R surprisingly vanish and the M - T feature is monotonically addressed by a hysteresis character only [e.g., below ~ 215 K in $x = 0.6$; inset, Fig. 3(b)]. In the recent study of the full solid solution of Yb(Fe,Mn)O₃ perovskites, very similar M - T hysteresis features to ours shown for $x = 0.5$ and 0.6 [inset, Fig. 3(b); those of $x = 0.7-0.9$ analogous to $x = 0.6$, thus not shown for simplicity] were also reported in the Mn-rich phases therein, whereas not further elaborated on in detail.¹⁵ Moreover, the isothermal M - H features of $x = 0.5$ and 0.6 [Fig. 3(c)] show a close resemblance to those acquired in DyFeO₃ single crystals below 4.2 K with $H \parallel c$ axis.^{16,32} At $T \leq 4.2$ K (i.e., below T_R), the Fe³⁺ spins in DyFeO₃ order in the collinear G_y -AFM type along the b axis, and the associated gentle M - H hysteresis in the single crystals, just like those in Fig. 3(c), has been unambiguously established to arise from a field-induced Fe³⁺-spin canting along the c axis,¹⁶ i.e., a field-induced WFM (FI-WFM) in the bc plane. Further considering that the phase of $x = 0.5$ antiferromagnetically orders along the b axis in G_y type at $T < T_R$ as well [inset, Fig. 3(b); also Ref. 14], its slight hysteresis in Fig. 3(c) could also correspond to a FI-WFM state in $x = 0.5$ below ~ 300 K, as denoted by $T_{N'}$ [inset, Fig. 3(b)] for differentiating from T_N in WFM ($G_x F_z$), and in $x = 0.6-0.9$ below $T_{N'}$ [see $x = 0.6$, Fig. 3(c)]. Otherwise, in WFM ($G_x F_z$), the reported M - H curve is characterized by a classical hysteresis loop with remnant M at zero field and the well-defined coercive field,¹⁵ both of which are absent in those shown in Fig. 3(c). Although

the onset of this proposed FI-WFM state in $x = 0.5$ was not documented in the previous report for DyFe_{1-x}Mn_xO₃ ($x = 0, 0.1-0.5$) powders,¹⁴ this observed characteristic in $x = 0.5$ intriguingly coincides with the effective orbital-ordered onset induced by the JT distortion at $x \sim 0.5$ [Figs. 2(b) and 2(c)]. Moreover, the correlated canted AFM ordering in $x = 0.5$, to the first approximations also in the bc plane like the case of DyFeO₃ (implying $D \parallel a$ axis; argued below),¹⁶ seems to entangle with the prominent lattice degree of freedom in the bc plane sublattice at $x \geq 0.5$ [Figs. 2(b) and 2(c)].

Upon increasing Mn from $x = 0$ to 0.5 [Fig. 4(a)], it has been known that the perturbation induced by Mn³⁺ spins to the anisotropic superexchange interactions in Fe³⁺ of DyFeO₃ results in the continuous decrease in T_N and M [Figs. 3(a) and 3(b)].¹⁴ The accompanied increase in T_R [$x = 0$ to 0.5 , Fig. 4(a)] deserves further investigations, since T_R is principally dictated by the effect of the magnetic anisotropy of Dy³⁺,³²⁻³⁴ of which the concentration remains, however, unchanged hereby. In DyFe_{1-x}Co_xO₃ ($x = 0-0.06$),³⁸ a similar increase in T_R with increasing Co was proposed to arise from the associated change in transition-metal anisotropic exchange fields, accounting for the increase in T_R from ~ 35 K ($x = 0$) to ~ 130 K ($x = 0.003$). Above $x = 0.003$, T_R turns to decrease in that material system and the consequence was only marginally addressed by the exchange-field arguments.³⁸ Obviously, the change in anisotropic exchange interactions alone can barely explain the dramatic T_R increase up to ~ 310 K observed in our $x = 0.5$ [Figs. 3(b) and 4(a); otherwise ~ 300 K in Ref. 14] despite the different material systems considered.³⁸ Such a high transition temperature could direct one to the necessity of considering anisotropy accompanied with the lattice and/or orbital degrees of freedom (i.e., JT distortion and/or orbital ordering), either of which is customarily stabilized above room temperature in rare-earth manganites,^{1-3,39} as currently revealed in the JT distortion, effective orbital-ordering onset, and predominance of the bc -plane sublattice in DyFe_{1-x}Mn_xO₃ at room temperature [Figs. 2(b) and 2(c)].

Figure 5(a) examines the lattice anisotropy specific to the local Dy environment in the solid solution. The eight NN-coordinated M (= Fe, Mn), previously viewed as four in ab projection [e.g., Fig. 4(c)], are doubly paired as M1-M4 now [inset, Fig. 5(a)] in accordance with the equivalence in the respective Dy-M lengths. In Fig. 5(a), the longest (shortest) Dy-M1 (Dy-M4) lying in the bc plane and the corresponding increase (decrease) towards $x = 1$, both induced by the JT distortion predominantly along the b axis [Fig. 2(b)], firmly unravel the anisotropy in the local Dy environment. The corresponding average local distortion [Fig. 5(a)] evaluated using the similar principle for Δ_d in Fig. 2(c) also envisages an increasing local anisotropy towards DyMnO₃. In Fig. 5(a), the effective orbital-ordered onset is revealed around $x \sim 0.5$ as well [see the slope crossover guided by dotted lines; also Fig. 2(c)]. In the solid solution, the predominance of the bc -plane sublattice [Figs. 2(b) and 2(c)] is, therefore, faithfully conveyed to the bc -plane anisotropy in the local Dy environment [Fig. 5(a)], and the electronic influence of this latter character on the M³⁺ magnetic sublattice has been suggested to be accomplished by the hybridizations between Dy $5d$ and M $3d$ states through the coordinated oxygen.¹⁷

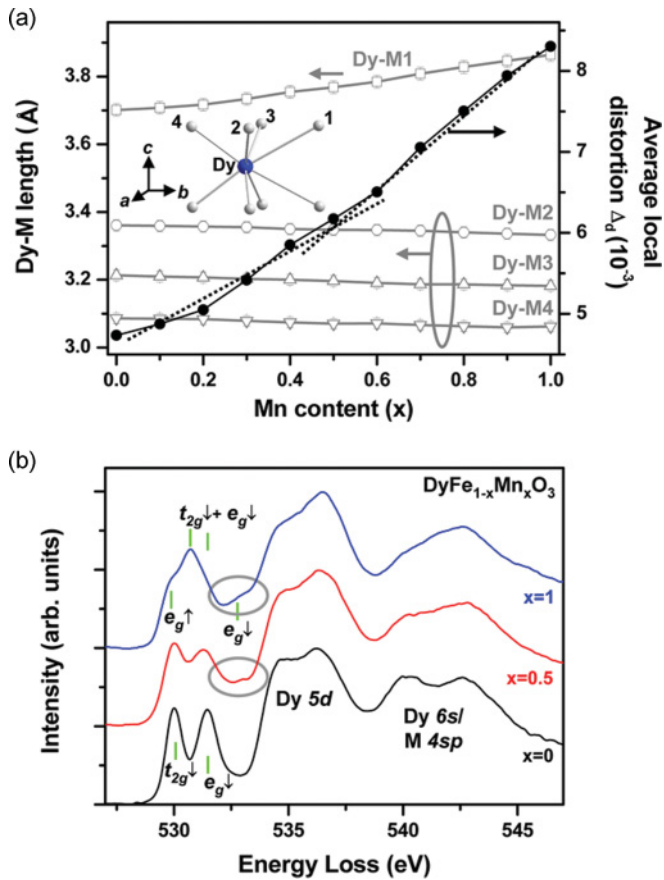


FIG. 5. (Color online) (a) The evaluation of the lattice anisotropy specific to the local Dy environment (inset; gray atom, M) through variations in the NN Dy-M lengths. The corresponding average distortion in the local Dy-M environment estimated using the similar principle for Δ_d in Fig. 2(c). Dotted lines guiding Δ_d signify the effective onset of orbital ordering around the slope crossover at $x \sim 0.5$ as shown in Fig. 2(c). Error bars: estimated standard deviations (0.5% of the corresponding data) derived from the respective Rietveld refinements. The error bars for Δ_d , though shown, are invisible in the scale of the figure. (b) The O K-edge EELS spectra in the solid solution ($x = 0, 0.5$, and 1), showing the dipole-forbidden transitions to M 3d, Dy 5d, and deep Dy/M levels as a result of the hybridizations with oxygen. Gray circle ($x = 0.5$ and 1): the oxygen-assisted M-3d-Dy-5d hybridizations through the spectral overlap around the $e_g \downarrow$ state.

Figure 5(b) shows the representative O K-edge EELS spectra in the solid solution ($x = 0, 0.5$, and 1). The three groups of dipole-forbidden transitions from O 1s to M 3d (528–533 eV), Dy 5d (533–538 eV), and deep Dy/M levels (>538 eV) are facilitated by the hybridizations with oxygen in the materials.^{20–22,25,40} A careful examination of the M-3d features in Fig. 5(b) reveals the triply (doubly) degenerate Fe-3d $t_{2g} \downarrow$ ($e_g \downarrow$) states in DyFeO_3 and the more complicated Mn-3d line shape contributed by $e_g \uparrow$, $t_{2g} \downarrow$, and $e_g \downarrow$ in DyMnO_3 .²⁵ Previous reports on the polarization-dependent O K edge in TbMnO_3 using an x-ray absorption technique have clearly determined that the partial DOS of $e_g \downarrow$ are most prominent along the a and b axes and significantly hybridize with R 5d states through the mediation of oxygen.⁴⁰ Figure 6(a) shows the calculated total and site-decomposed DOS of DyMnO_3

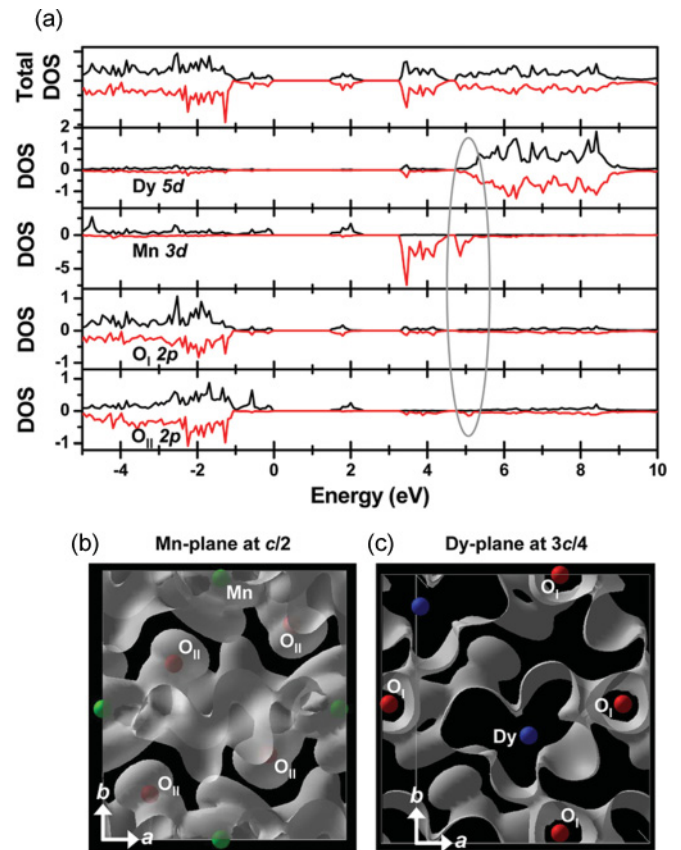


FIG. 6. (Color online) (a) The total and site-decomposed DOS of DyMnO_3 calculated with the GGA + U method. The energy zero denotes the Fermi level. Black (red), the majority (minority) spin states. [(b) and (c)] The three-dimensional isocharge density contour projected onto the Mn plane at $c/2$ and the Dy plane at $3c/4$ with the c -projected ranges of 0.34–0.66 and 0.6–0.8 c , respectively. The electron density surfaces were derived from the calculated energy range of 4.6–5.2 eV in (a), gray ellipsoid, which corresponds to Mn $e_g \downarrow$ and partly Dy 5d and O 2p bands. The overlap of the derived electron densities between Mn and Dy revealed in (b) and (c) gives direct evidence for the hybridizations between the corresponding electronic states.

using the approach of generalized gradient approximation plus on-site Coulomb interaction U (GGA + U), which was performed using the Vienna *ab initio* simulation package with the full-potential projected augmented wave method.^{25,40} In the calculations, an energy of 5 eV was used for U and an intra-atomic exchange energy (J) of 0.87 eV was exploited for the Mn 3d electrons. Figures 6(b) and 6(c) exhibit the isocharge density contour derived from the energy range of 4.6–5.2 eV in Fig. 6(a) (gray ellipsoid), which corresponds to Mn $e_g \downarrow$ and partly Dy 5d and O 2p bands. In Figs. 6(b) and 6(c), the overlap of the derived electron densities between Mn and Dy, mediated by oxygen, gives direct evidence for the hybridizations between R 5d and Mn $e_g \downarrow$ states also in DyMnO_3 compared to the established case of TbMnO_3 .⁴⁰ The experimental, spectroscopic observation of such hybridizations in DyMnO_3 is reflected in the spectral-weight overlap between Mn 3d and Dy 5d states around $e_g \downarrow$ [gray circle for $x = 1$, Fig. 5(b)], also evidenced in Fig. 6(a) (DOS, gray ellipsoid;

also total DOS). While the O K edge of $x = 0.5$ resembles the intermixing between DyFeO₃ and DyMnO₃ [Fig. 5(b)], this spectral hybridization signature for M 3d and Dy 5d states is also observed (gray circle for $x = 0.5$; also the case for $x = 0.1$ –0.4 and 0.6–0.9, not shown). The visible increase in the Dy-5d spectral widths from $x = 0$ to 1 [Fig. 5(b)] indicates a reduction of the electron lifetime typically due to the creation of holes thereby by hybridizations,²⁰ giving additional evidence for the above Dy-M electronic interactions. The full electronic characterizations of the solid solution by core-level spectroscopy will be published elsewhere. Indeed, the increasing local Dy anisotropy [Fig. 5(a)] and the correlated electronic hybridizations [Fig. 5(b)] provide an indispensable view angle of the increasing Dy-M electronic interaction anisotropy in the bc plane for the growingly elevated T_R [$x = 0$ –0.5, Fig. 4(a)], which is difficult to understand using arguments of changes in anisotropic exchange fields alone.³⁸

Further from the merging tendency of T_N and T_R in Fig. 4(a) ($x = 0$ –0.5), WFM ($G_x F_z$) and AFM (G_y) behave, in effect, as degenerate states when close to $x = 0.5$ and seem to meet a triple point at $x \sim 0.5$ in the phase diagram with the PM, WFM, and AFM states being qualitatively degenerate hereby, facilitating effective competitions among them and potentially giving rise to electronic frustration. The FI-WFM onset [$x = 0.5$, Figs. 3(c) and 4(a)] upon such a frustration at $x \sim 0.5$ reveals the electronic subtlety of this previously unexplored magnetic ground state in $x = 0.5$,¹⁴ of which the stabilization is clearly entangled with the predominance of the bc -plane sublattice [most prominent at $x \geq 0.5$, Figs. 2(b) and 2(c)] and the increasing Dy-M electronic interaction anisotropy in the bc plane (Figs. 5 and 6), both correlated with the JT distortion. The effective orbital-ordered onset in the ab plane at $x \geq 0.5$ induced by the JT distortion [Figs. 2(b) and 2(c)] is also important, since it would favor a spin orientation predominantly along the b axis taking into account the orbital ordering in DyMnO₃ [inset, Fig. 2(b)] facilitating a primarily b -oriented spin arrangement.^{4,6–9} The conventional DM relation of $D \parallel b$ axis for WFM [$G_x F_z$, Fig. 4(a)] is thus quenched in this FI-WFM onset at $x = 0.5$, because the principally b -aligned spins ($S_{i,j}$) in $x = 0.5$ would tend to be parallel with the associated D vector, whereas $D \perp S_{i,j}$ for the DM interaction.³⁵ Only the previously hidden condition of $D \parallel a$ axis can account for this FI-WFM state now, justifying the presumed canted AFM ordering in the bc plane for $x = 0.5$ –0.9 [schematized in Fig. 4(c)], G -type ordering along the b axis and canting along the c axis].

Under the presence of the aforementioned electronic frustration at $x \sim 0.5$, the entrance of this unexpected condition of $D \parallel a$ axis in $x = 0.5$ [i.e., FI-WFM; Fig. 4(c)] can readily be understood as a delicate electronic compromise assisted by the coupling of the predominant bc -plane sublattice, the increasing Dy-M electronic interaction anisotropy in the bc plane, and the effective orbital ordering in the ab plane. The intimate coupling of these anisotropies from the various degrees of freedom (lattice, orbital, and correlated electronic characters) favors a noncollinear magnetic ordering in the bc plane (FI-WFM). At $x > 0.5$, the disappearances of T_N and T_R [Fig. 4(a)] designating rather the respective spin degrees of freedom in the ac plane and collinearly along the b axis may qualitatively be understood as an effect of

the mismatch with the primary magnetic anisotropy in the bc plane. The continuous decrease in the FI-WFM transition temperature (T_N) from $x = 0.6$ to 0.9 [Fig. 4(a)], however, points to the weakening of this delicately settled magnetic ground state of FI-WFM. With the increase in Mn from $x = 0.6$ to 0.9, the effective orbital ordering in the ab plane and the JT distortion primarily along the b axis become more obvious [Figs. 2(b) and 2(c)] and would tend to establish an in- (ab) plane electronic anisotropy as in the case of the parent phase of DyMnO₃,^{4,5,7,9} potentially competing with the Dy-M electronic interaction anisotropy in the bc plane [Figs. 5(a) and 5(b)]. This in- (ab) and out-of-plane electronic competition could be disadvantageous for the noncollinear ordering of FI-WFM in the bc plane and provides a qualitative understanding for the decrease in T_N with increasing Mn [$x = 0.6$ –0.9, Fig. 4(a)]. In DyMnO₃ characterized by the most prominent orbital ordering in the solid solution [Figs. 2(b) and 2(c)], the FI-WFM state is indeed missing as reported,^{4,5,13} supporting our above-proposed electronic competition for reduced T_N . Furthermore, DyMnO₃ is well known to display a sinusoidally modulated incommensurate collinear AFM ordering along the b axis below ~ 40 K [Fig. 4(a)], followed by a transition to the incommensurate spiral ground state in the bc plane at ~ 18 K due to the DM interaction or the spin current mechanism (a DM counterpart without oxygen displacements).^{4–11} This DM interaction or eventually the spin current mechanism in DyMnO₃ intriguingly directs one to the relation of $D \parallel a$ axis as observed in our $x = 0.5$ –0.9, though not specifically pointed out in those reports.^{7–11} Moreover, it was experimentally demonstrated that the Dy magnetic anisotropy in DyMnO₃ is primarily along the b axis and the anisotropic Dy-Mn magnetic interaction is significant,⁷ both of which are qualitatively consistent with our Dy-M derivations in Figs. 5 and 6. The DM relation of $D \parallel a$ axis was largely ignored before for $Pbnm$ and the corresponding hidden noncollinear magnetic ground state is revived here (FI-WFM, $x = 0.5$ –0.9) through interplays of the lattice, orbital, and electronic-interaction anisotropies induced by the JT distortion in the solid solution with high Mn concentrations.

Indeed, it remains unclear about the exact commensurability between the magnetic and structural sublattices of the FI-WFM states in $x = 0.5$ –0.9 and the underlying origin for the sudden changes in magnetic ground states from FI-WFM ($x = 0.9$) to incommensurate spiral ordering ($x = 1$). A detailed calculation considering all possibly involved exchange interactions and/or orbital-coupled pseudospins should shed light on the microscopic backgrounds addressing both subtleties. Nevertheless, such a theoretical effort is a separate dedicated issue on its own and the present work focuses on the experimental aspects of the solid solution.

IV. CONCLUSION

In summary, the JT distortion characteristic to Mn³⁺ induces two prominent effects on the respective lattice and orbital degrees of freedom in DyFe_{1-x}Mn_xO₃ ($x = 0$ –1), the predominance of the bc -plane sublattice upon increasing Mn concentrations, and the effective orbital ordering in the ab plane at $x \geq 0.5$. The former character gives rise to a Dy-M electronic interaction anisotropy primarily in the bc plane

and the latter feature facilitates a primarily b -aligned spin orientation and a growing in- (ab) plane electronic anisotropy at $x \geq 0.5$. At the half-doping level of $x = 0.5$, these electronic impacts of the lattice and orbital degrees of freedom envisage intriguing interplays and the associated frustration is comprised by the onset of a hidden FI-WFM magnetic ground state (canted AFM ordering in the bc plane) dictated by the DM interaction of $D \parallel a$ axis, not documented before in this material system.¹⁴ At higher Mn concentrations ($x = 0.6$ – 0.9), the FI-WFM state persists, whereas the corresponding transition temperature decreases with increasing Mn due qualitatively to the electronic competitions between the Dy-M interaction anisotropy in the bc plane and the orbital-ordered-induced electronic anisotropy in the ab plane. In DyMnO_3 featuring the most prominent ab -plane electronic anisotropy assisted by the promising staggered orbital ordering, the FI-WFM state

accordingly disappears and is replaced with the well-known magnetic ground state of an incommensurate spiral ordering in the bc plane.^{4–11} Indeed, the complex interplays of the lattice and orbital degrees of freedom, induced by the JT distortion, with the correlated electronic anisotropies give rise to the rich magnetic phase diagram [Fig. 4(a)], which was not thoroughly explored before.¹⁴

ACKNOWLEDGMENTS

The authors thank Y. K. Kuo (Department of Physics, National Dong Hwa University, Taiwan) and J. M. Chen (National Synchrotron Radiation Research Center, Taiwan) for helpful discussions. This work was supported by the National Science Council of Taiwan and the National Taiwan University Excellence Project.

*Corresponding author: chumingwen@ntu.edu.tw

¹M. Imada, A. Fujimori, and Y. Tokura, *Rev. Mod. Phys.* **70**, 1039 (1998).

²E. Pavarini and E. Koch, *Phys. Rev. Lett.* **104**, 086402 (2010).

³Y. Tokura and N. Nagaosa, *Science* **288**, 462 (2000).

⁴T. Kimura, S. Ishihara, H. Shintani, T. Arima, K. T. Takahashi, K. Ishizaka, and Y. Tokura, *Phys. Rev. B* **68**, 060403 (2003).

⁵M. Tachibana, T. Shimoyama, H. Kawaji, T. Atake, and E. Takayama-Muromachi, *Phys. Rev. B* **75**, 144425 (2007).

⁶M. Kenzelmann, A. B. Harris, S. Jonas, C. Broholm, J. Shcefer, S. B. Kim, C. L. Zhang, S.-W. Cheong, O. P. Vajk, and J. W. Lynn, *Phys. Rev. Lett.* **95**, 087206 (2005).

⁷N. Aliouane, O. Prokhnenko, R. Feyerherm, M. Mostovoy, J. Stremper, K. Habicht, K. C. Rule, E. Dudzik, A. U. B. Wolter, A. Maljuk, and D. N. Argyriou, *J. Phys.: Condens. Matter* **20**, 434215 (2008).

⁸T. Arima, A. Tokunaga, T. Goto, H. Kimura, Y. Noda, and Y. Tokura, *Phys. Rev. Lett.* **96**, 097202 (2006).

⁹S. Dong, R. Yu, S. Yunoki, J.-M. Liu, and E. Dagotto, *Phys. Rev. B* **78**, 155121 (2008).

¹⁰I. A. Sergienko and E. Dagotto, *Phys. Rev. B* **73**, 094434 (2006).

¹¹H. Katsura, N. Nagaosa, and A. V. Balatsky, *Phys. Rev. Lett.* **95**, 057205 (2005).

¹²T. Kimura, T. Goto, H. Shintani, K. Ishizaka, T. Arima, and Y. Tokura, *Nature (London)* **426**, 55 (2003).

¹³T. Goto, T. Kimura, G. Lawes, A. P. Ramirez, and Y. Tokura, *Phys. Rev. Lett.* **92**, 257201 (2004).

¹⁴Y. Nagata, S. Yashiro, T. Mitsuhashi, A. Koriyama, Y. Kawashima, and H. Samata, *J. Magn. Magn. Mater.* **237**, 250 (2001).

¹⁵Y.-H. Huang, M. Karppinen, N. Imamura, H. Yamauchi, and J. B. Goodenough, *Phys. Rev. B* **76**, 174405 (2007).

¹⁶Y. Tokunaga, S. Iguchi, T. Arima, and Y. Tokura, *Phys. Rev. Lett.* **101**, 097205 (2008).

¹⁷A. Stroppa, M. Marsman, G. Kresse, and S. Picozzi, *New J. Phys.* **12**, 093026 (2010).

¹⁸M.-W. Chu, Y. Shingaya, and T. Nakayama, *Appl. Phys. A* **86**, 101 (2007).

¹⁹M.-W. Chu, M. T. Caldes, Y. Piffard, A.-M. Marie, E. Gautier, O. Joubert, M. Ganne, and L. Brohan, *J. Solid State Chem.* **172**, 389 (2003).

²⁰J.-S. Kang, H. J. Lee, G. Kim, D. H. Kim, B. Dabrowski, S. Kolesnik, H. Lee, J.-Y. Kim, and B. I. Min, *Phys. Rev. B* **78**, 054434 (2008).

²¹M. Haruta, H. Kurata, H. Komatsu, Y. Shimakawa, and S. Isoda, *Phys. Rev. B* **80**, 165123 (2009).

²²D. A. Eustace, D. W. McComb, and A. J. Craven, *Micron* **41**, 547 (2010).

²³R. D. Shannon, *Acta Crystallogr., Sect. A: Cryst. Phys., Diffr., Theor. Gen. Crystallogr.* **32**, 751 (1976).

²⁴V. A. Streltsov and N. Ishizawa, *Acta Crystallogr., Sect. B: Struct. Sci.* **55**, 1 (1999).

²⁵J. M. Chen, Z. Hu, H. T. Jeng, Y. Y. Chin, J. M. Lee, S. W. Huang, K. T. Lu, C. K. Chen, S. C. Haw, T. L. Chou, H.-J. Lin, C. C. Shen, R. S. Liu, A. Tanaka, L. H. Tjeng, and C. T. Chen, *Phys. Rev. B* **81**, 201102(R) (2010).

²⁶J. B. Goodenough, *Phys. Rev.* **100**, 564 (1955).

²⁷N. E. Brese and M. O'Keefe, *Acta Crystallogr., Sect. B: Struct. Sci.* **47**, 192 (1991).

²⁸J. Kanamori, *J. Appl. Phys.* **31**, 14S (1960).

²⁹J.-S. Zhou and J. B. Goodenough, *Phys. Rev. B* **77**, 132104 (2008).

³⁰J. Rodríguez-Carvajal, M. Hennion, F. Moussa, and A. H. Moudden, *Phys. Rev. B* **57**, R3189 (1998).

³¹M. O'Keefe and B. G. Hyde, *Acta Crystallogr., Sect. B: Struct. Crystallogr. Cryst. Chem.* **33**, 3802 (1977).

³²G. Gorodetsky, B. Sharon, and S. Stickmen, *J. Appl. Phys.* **39**, 1371 (1968).

³³R. L. White, *J. Appl. Phys.* **40**, 1061 (1969).

³⁴R. D. Pierce, R. Wolfe, and L. G. Van Uitert, *J. Appl. Phys.* **40**, 1241 (1969).

³⁵T. Moriya, *Phys. Rev.* **120**, 91 (1960).

³⁶*International Table for Crystallography Volume D: Physical Properties of Crystals*, 1st ed., edited by A. Authier (Wiley, UK, 2003).

³⁷*International Table for Crystallography Volume A: Space-Group Symmetry*, 5th ed., edited by Th. Hahn (Springer, Berlin, 2005).

- ³⁸L. Holmes, L. G. Van Uitert, and R. Hecker, *J. Appl. Phys.* **42**, 657 (1971).
- ³⁹M. V. Mostovoy and D. I. Khomskii, *Phys. Rev. Lett.* **92**, 167201 (2004).

- ⁴⁰J. M. Chen, J. M. Lee, C. K. Chen, T. L. Chou, K. T. Lu, S. C. Haw, K. S. Liang, C. T. Chen, H. T. Jeng, S. W. Huang, T. J. Yang, C. C. Shen, R. S. Liu, J. Y. Lin, and Z. Hu, *Appl. Phys. Lett.* **94**, 044105 (2009).